SUBMILLIMETER OBSERVATIONS OF DENSE CLUMPS IN THE INFRARED DARK CLOUD G049.40–00.01

Miju Kang[1], Minho Choi[1], John H. Bieging[2], Jeonghee Rho[3], Jeong-Eun Lee[4], and Chao-Wei Tsai[5]

[1] Korea Astronomy and Space Science Institute, 776 Daedeokdaero, Yuseong, Daejeon 305-348, Republic of Korea; mjkang@kasi.re.kr
[2] Steward Observatory, University of Arizona, 933 North Cherry Avenue, Tucson, AZ 85721, USA
[3] SOFIA Science Center, USRA/NASA Ames Research Center, Moffet Field, CA 94035, USA
[4] Department of Astronomy and Space Science, Kyung Hee University, Yongin, Gyeonggi 446-701, Republic of Korea
[5] Infrared Processing and Analysis Center, California Institute of Technology, Pasadena, CA 91125, USA

ABSTRACT

We obtained 350 and 850 μm continuum maps of the infrared dark cloud G049.40–00.01. Twenty-one dense clumps were identified within G049.40–00.01 based on the 350 μm continuum map with an angular resolution of about 9$\overset{\prime\prime}{.}$6. We present submillimeter continuum maps and report physical properties of the clumps. The masses of clumps range from 50 to 600 $M_\odot$. About 70% of the clumps are associated with bright 24 μm emission sources, and they may contain protostars. The two most massive clumps show extended, enhanced 4.5 μm emission indicating vigorous star-forming activity. The clump-size–mass distribution suggests that many of them are forming high-mass stars. G049.40–00.01 contains numerous objects in various evolutionary stages of star formation, from pre-protostellar clumps to H II regions.

Key words: ISM: individual objects (G049.40–00.01) – ISM: structure – stars: formation

1. INTRODUCTION

Massive stars form in cold, dense molecular clouds and in clusters (Lada & Lada 2003). Infrared dark clouds (IRDCs) are complexes of cold ($T < 20$ K), dense ($n > 10^4$ cm^{-3}) molecular gas, some of which are believed to be the progenitors of massive stars and star clusters (Egan et al. 1998; Carey et al. 1998; Rathborne et al. 2006). IRDCs were identified as dark extinction features because the cold dust in IRDCs absorbs the bright mid-infrared emission of the Galactic plane (Egan et al. 1998). Cold, dense molecular gas and dust in IRDCs were confirmed based on observations at millimeter and submillimeter wavelengths (Carey et al. 1998, 2000; Rathborne et al. 2005, 2006). IRDCs fragment into multiple cores (Beuther & Henning 2009). Battersby et al. (2010) divided the evolutionary sequence of IRDCs into four stages from a quiescent clump to an embedded H II region by combining millimeter–centimeter continuum data and spectroscopic data of the HCO$^+$ and N$_2$H$^+$ lines. Some IRDCs are thought to be good targets for investigating the initial conditions of massive star formation (Beuther et al. 2007; Rathborne et al. 2006; Chambers et al. 2009).

Recently, Kang et al. (2009) cataloged embedded young stellar objects (YSOs) near W51 using the data from the Galactic Legacy Infrared Mid-Plane Survey Extraordinaire (GLIMPSE I; Benjamin et al. 2003) and the Mid-infrared Imaging Photometer for Spitzer Galactic plane Survey (MIPSGAL; Carey et al. 2009). A total of 35 YSOs have been found over the area of $0\overset{\circ}{.}15 \times 0\overset{\circ}{.}14$ centered at $l = 49\overset{\circ}{.}4$ and $b = 0\overset{\circ}{.}00$. This region corresponds to MSXDC G049.40–00.01 identified from the *Midcourse Space Experiment* 8 μm data (Simon et al. 2006a). (Hereafter we refer to the region as G049.40–00.01, after dropping the MSXDC label.) G049.40–00.01 includes three *Spitzer* dark clouds cataloged with the GLIMPSE 8 μm data (Peretto & Fuller 2009). G049.40–00.01 is associated with the CO emission showing a velocity peak at $V_{\rm LSR} = 61$ km s^{-1}, which is a part of the "cluster" region near the active star-forming complex W51 (Kang et al. 2010). Recent measurements of the distance to W51 gave $5.41^{+0.31}_{-0.28}$ kpc (Sato et al. 2010),

$5.1^{+2.9}_{-1.4}$ kpc (Xu et al. 2009), and 6.1 ± 1.3 kpc (Imai et al. 2002). Here, we adopt 6 kpc as the distance to G049.40–00.01 (with an uncertainty of ∼1 kpc), for consistency with previous works. The peak H$_2$ column density estimated from the ^{13}CO $J = 1$–0 line observations is 1.6×10^{22} cm^{-2} (Simon et al. 2006b). Two compact H II regions were identified based on the *Spitzer* data (Phillips & Ramos-Larios 2008).

In this paper, we present the results of submillimeter observations of the IRDC G049.40–00.01 using the Submillimeter High Angular Resolution Camera II (SHARC-II) at the Caltech Submillimeter Observatory (CSO). We describe details of the observations and data in Section 2. Then we report the results in Section 3 and discuss the physical properties of the clumps in G49.40–00.01 in Section 4. We summarize the main results in Section 5.

2. OBSERVATIONS AND DATA

The observations were made on 2010 May 10 and 15 at the CSO 10.4 m telescope near the summit of Mauna Kea, Hawaii. We used the bolometer camera SHARC-II (Dowell et al. 2003). The instrument resolution of SHARC-II is 8$\overset{\prime\prime}{.}$0 at 350 μm and 19$\overset{\prime\prime}{.}$4 at 850 μm. The Dish Surface Optimization System was used to correct the dish surface for static imperfections and deformations due to gravitational forces as the dish moves in elevation (Leong et al. 2006). We obtained five scans at 350 μm for a total integration time of 50 minutes in moderate weather ($\tau_{225\,{\rm GHz}} \approx 0.046$–0.068) and fourteen scans at 850 μm for a total integration time of 140 minutes in moderate weather ($\tau_{225\,{\rm GHz}} \approx 0.053$–0.078). Pointing and calibration scans were taken on an hourly basis on strong submillimeter sources: Neptune, Arp 220, IRAS 16293–2422, CRL 2688, W75N, and K 3-50. The data were reduced using version 2.01-2 of the software package CRUSH (Comprehensive Reduction Utility for SHARC-II; Kovács 2006). The final maps were smoothed to angular resolutions of FWHM = 9$\overset{\prime\prime}{.}$61 at 350 μm and 23$\overset{\prime\prime}{.}$32 at 850 μm.

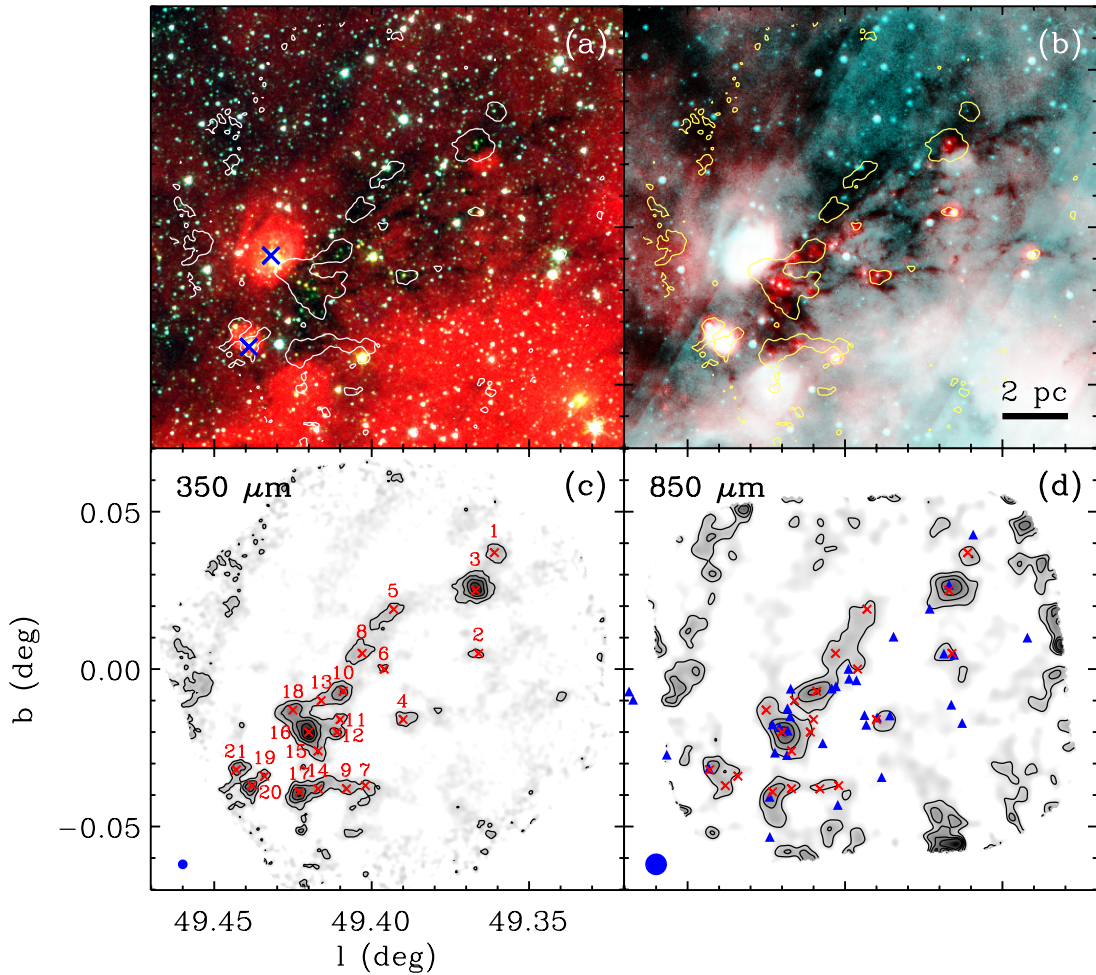The *Spitzer* data presented here are the GLIMPSE and MIPSGAL data. GLIMPSE and MIPSGAL are legacy programs

Figure 1. Infrared and submillimeter maps of the IRDC G049.40–00.01. (a) IRAC three-color composite ($8.0\,\mu$m in red, $4.5\,\mu$m in green, and $3.6\,\mu$m in blue) image overlaid with the 4σ contour of the $350\,\mu$m map. Two large crosses mark the compact H II regions PR 29 and 30, from north to south (Phillips & Ramos-Larios 2008). (b) IRAC and MIPS two-color composite ($8.0\,\mu$m in cyan and $24\,\mu$m in red) image. The scale bar indicates 2 pc. (c) SHARC-II $350\,\mu$m image (both gray scale and contours). The compact sources (clumps) are labeled and marked by small crosses. Contour levels are 4, 8, 12, 16, and 20×0.09 (1σ) Jy beam^{-1}. (d) SHARC-II $850\,\mu$m image. Contour levels are 3, 6, 9, and 12×0.05 (1σ) Jy beam^{-1}. The crosses mark the positions of the $350\,\mu$m clumps. The filled triangles mark the YSOs from Kang et al. (2009). The FWHM resolutions of the SHARC-II maps are indicated in the bottom left corners. The extraneous contours (noisy areas) near the edges of the SHARC-II maps should be ignored.

covering the inner Galactic plane at 3.6, 4.5, 5.8, and $8.0\,\mu$m with the Infrared Array Camera (IRAC; Fazio et al. 2004) and at 24 and $70\,\mu$m with the Multiband Imaging Photometer for *Spitzer* (MIPS; Rieke et al. 2004), respectively.

3. RESULTS

Figure 1 shows the *Spitzer* IRAC, MIPS, and SHARC-II 350 and $850\,\mu$m maps toward the IRDC G049.40–00.01. In the IRAC composite map (Figure 1(a)), a dark filamentary structure is seen in absorption against the background emission. The bright features in the IRAC composite map are two H II regions and bright diffuse emission from the active star-forming region W51 to the south. The spatial distribution of the dark filamentary structure agrees well with the distribution of the $350\,\mu$m emission. Figure 1(b) shows the two-color composite (IRAC $8.0\,\mu$m in cyan and MIPS $24\,\mu$m in red) image, overlaid with the $350\,\mu$m emission map. Some regions of G049.04–00.01 are still dark at $24\,\mu$m, implying low temperature and high column density. There are also many bright $24\,\mu$m point-like sources located within the IRDC. The dark features of the IRDC seen in the *Spitzer* maps appear in emission in the 350 and

$850\,\mu$m maps (Figures 1(c) and (d)) because their cold thermal dust emission peaks at millimeter/submillimeter wavelengths. The bright clumps in the $350\,\mu$m map are well aligned with the $24\,\mu$m peaks, which suggests that the $24\,\mu$m sources are central stars of these dense clumps. The distribution of $850\,\mu$m emission is very similar to that of $350\,\mu$m emission except for the unresolved details with the relatively large beam of the $850\,\mu$m map. The maximum flux densities are 1.96 ± 0.09 and 0.64 ± 0.05 Jy beam^{-1} at 350 and $850\,\mu$m, respectively.

A total of 21 sources were identified as compact clumps for which peak flux densities are greater than the 4σ level in the $350\,\mu$m continuum map by eye. When a peak is located close to another one, it is considered an independent peak if the peak intensity is higher than the intensity at the interface between them by the 1σ level or larger and if their separation is larger than the beam size. Table 1 lists the peak positions, peak flux densities, $350\,\mu$m total flux density, size, number of associated $24\,\mu$m sources, and associated YSOs of each clump. The total flux density at $350\,\mu$m is measured from the emission in the circumscribed box of the 2σ contour. In crowded areas, the saddle point between adjacent clumps is

Table 1
Submillimeter Continuum Source Parameters

| Source | Peak Position[a] | | Peak Flux[b] | | Total Flux | Size[c] | 24 μm | Associated |
	l (deg)	b (deg)	850 μm (Jy beam^{-1})	350 μm (Jy beam^{-1})	at 350 μm (Jy)	($'' \times ''$)	Sources[d]	YSOs[e]
1...	49.361	0.037	0.30	0.58	3.4 ± 0.4	21 × 21	...	
2...	49.366	0.005	0.24	0.54	1.6 ± 0.3	21 × 8	2	345, 348
3...	49.367	0.025	0.58	1.75	11.8 ± 1.1	22 × 19	2	346
4...	49.390	−0.016	0.26	0.54	2.5 ± 0.2	26 × 21	3	362, 366, 367
5...	49.393	0.019	0.23	0.55	5.1 ± 1.6	53 × 19	...	
6...	49.396	−0.000	0.23	0.41	1.2 ± 0.1	16 × 15	1	
7...	49.401	−0.036	...	0.54	1.6 ± 0.2	22 × 16	...	
8...	49.403	0.005	0.27	0.56	4.4 ± 0.6	48 × 23	...	
9...	49.408	−0.038	0.19	0.68	2.3 ± 0.3	29 × 13	1	
10...	49.409	−0.007	0.48	1.09	5.5 ± 1.1	21 × 18	3	
11...	49.410	−0.016	...	0.63	1.4 ± 0.2	16 × 11	...	
12...	49.412	−0.020	...	0.99	2.2 ± 0.1	20 × 11	1	
13...	49.416	−0.010	...	0.57	1.4 ± 0.3	21 × 11	1	
14...	49.418	−0.038	...	0.88	3.4 ± 0.3	29 × 13	1	
15...	49.417	−0.027	...	0.70	2.1 ± 0.5	14 × 13	...	
16...	49.420	−0.021	0.65	1.96	13.3 ± 0.8	27 × 20	3	409, 414, 419
17...	49.423	−0.040	0.41	1.44	5.6 ± 0.8	24 × 17	1	421
18...	49.425	−0.013	0.27	1.02	4.3 ± 0.3	33 × 16	1[f]	
19...	49.434	−0.034	0.21	0.72	1.2 ± 0.3	13 × 7	...	
20...	49.439	−0.038	0.26	1.31	3.4 ± 0.9	14 × 12	1[f]	
21...	49.443	−0.032	0.40	0.94	2.3 ± 0.4	21 × 17	1	438

Notes.
[a] Peak position in the 350 μm image.
[b] Uncertainties are 0.05 and 0.09 Jy beam^{-1} at 850 and 350 μm, respectively.
[c] Deconvolved FWHM size of each clump in the 350 μm map. The first number is the size along the major axis (longest diameter) and the second number is the size along the direction perpendicular to the major axis.
[d] Number of 24 μm point sources within the size of each clump.
[e] YSO number in Table 2 of Kang et al. (2009).
[f] Associated with an H II region.

used to limit the area for total flux measurements. The size represents the FWHM, deconvolved with the beam. In crowded areas, the intensity at the saddle point between adjacent clumps can be higher than the half-maximum intensity. In this case, we give the distance to the saddle point from the peak position as a size (in the direction to the adjacent clump). Column 8 lists the number of all 24 μm point sources detected with significant signal-to-noise ratios (S/N > 4). Column 9 lists the YSOs in Kang et al. (2009). They used a detection criterion of S/N > 7 at 24 μm to identify YSOs. The peak fluxes at 850 μm are measured only for the clumps having 850 μm peaks within the size boundaries of the 350 μm sources as described above. Table 2 lists the 850 μm total flux densities. For many clumps the 850 μm total flux cannot be measured individually because of crowding.

4. DISCUSSION

4.1. Physical Parameters

Continuum emission at 350 μm is sensitive to dust temperature, and the mass of molecular gas estimated from the 350 μm flux density depends on the assumed dust temperature that varies with the presence or absence of central heating by embedded protostars. The clumps without detectable 24 μm sources may be pre-protostellar (harboring no protostar). Hennemann et al. (2009) derived dust temperatures of 22 and 15 K for cores with and without 24 μm sources, respectively. Stutz et al. (2010) found that the dust temperatures are ~17.7 K near the protostar and ~10.6 K for the starless core in the Bok globule CB 244.

Table 2
Total Flux at 850 μm

Sources	Total Flux (Jy)
1...	0.30 ± 0.05
2...	0.29 ± 0.13
3...	1.03 ± 0.15
4...	0.26 ± 0.05
5, 6, 8...	0.98 ± 0.18
7, 9...	0.22 ± 0.12
10, 13...	0.79 ± 0.15
11, 12, 15, 16, 18...	1.44 ± 0.18
14, 17...	0.73 ± 0.15
19, 20, 21...	0.51 ± 0.14

Notes. For crowded areas, the total flux densities of each area are listed.

Pre-protostellar and protostellar cores in the IRDC G011.1–0.12 have core temperatures of 22 K (Henning et al. 2010). Wilcock et al. (2011) derived temperatures of 8–11 K at the center of the cores and 18–28 K at the surface using radiative transfer models of IRDC seen in *Herschel* observations. Peretto et al. (2010) reported that IRDCs are not isothermal, showing that the dust temperature decreases significantly within IRDCs, from background temperatures of 20–30 K to minimum temperatures of 8–15 K within the clouds. In this paper, we assume a dust temperature of 15 K for simplicity and for ease of comparison with Kauffmann & Pillai (2010; see Section 4.3).

Table 3
Properties of the Clumps

Source	M_{total}[a] $(M_\odot)$	M_{FWHM}[b] $(M_\odot)$	Concentration
1...	154 ± 18	149 ± 27	0.65 ± 0.18
2...	73 ± 14	54 ± 20	0.73 ± 0.44
3...	536 ± 50	354 ± 75	0.77 ± 0.05
4...	113 ± 9	127 ± 14	0.65 ± 0.21
5...	232 ± 73	226 ± 109	0.78 ± 0.54
6...	54 ± 5	58 ± 7	0.57 ± 0.17
7...	73 ± 9	88 ± 14	0.50 ± 0.08
8...	200 ± 27	217 ± 41	0.55 ± 0.09
9...	104 ± 14	99 ± 20	0.59 ± 0.08
10...	250 ± 50	182 ± 75	0.72 ± 0.13
11...	64 ± 9	60 ± 14	0.50 ± 0.07
12...	100 ± 5	103 ± 7	0.64 ± 0.17
13...	64 ± 14	64 ± 20	0.39 ± 0.06
14...	154 ± 14	171 ± 20	0.69 ± 0.23
15...	95 ± 23	90 ± 34	0.62 ± 0.13
16...	604 ± 36	455 ± 54	0.67 ± 0.03
17...	254 ± 36	242 ± 54	0.71 ± 0.14
18...	195 ± 14	231 ± 20	0.54 ± 0.05
19...	54 ± 14	61 ± 20	0.62 ± 0.08
20...	154 ± 41	139 ± 61	0.64 ± 0.04
21...	104 ± 18	131 ± 27	0.65 ± 0.08

Notes. The mass is based on the total flux density at $350\,\mu$m assuming $T_d = 15$ K. If $T_d = 10$ K, multiply by 4.1. If $T_d = 20$ K, multiply by 0.47.
[a] Mass within the 2σ contour.
[b] Mass within the FWHM boundary with the opacity scaled by 1/1.5.

The masses of the submillimeter clumps in G049.40−00.01 were calculated using the $350\,\mu$m flux densities. The mass can be estimated by $M = F_\nu D^2/\kappa_\nu B_\nu(T_d)$, where F_ν is the flux density at $350\,\mu$m, D is the distance to the source, B_ν is the Planck function, T_d is the dust temperature, and κ_ν is the dust mass opacity. The value of κ_ν at $350\,\mu$m used to calculate the masses is 5.91 cm^2 g^{-1}, from the coagulated dust model with thin ice mantles of Ossenkopf & Henning (1994). Table 3 lists the total mass within the 2σ contour. The representative masses listed in Table 3 were calculated using a uniform temperature of 15 K. These masses can be underestimates for colder clumps (those without a $24\,\mu$m source) and overestimates for hotter clumps (those with $24\,\mu$m sources). Different assumptions on the dust temperature can increase or decrease the mass estimate by a factor of ∼3 (see the footnote to Table 3). The uncertainty of the mass caused by the uncertainty of the distance is ∼30%. The sum of the clump masses is ∼3600 $M_\odot$.

4.2. Comparison with Simple Models

The clumps in G049.40−00.01 could be produced by gravitational fragmentation, and some simple quantities can be calculated to check the consistency. The average surface density is ∼0.04 g cm^{-2} for the area within the 1σ contour in the $350\,\mu$m map. With this surface density and the assumed dust temperature of 15 K, the critical wavelength of an isothermal, infinite, self-gravitating cylinder is $\lambda_c \approx 0.3$ pc, and the corresponding critical mass is $M_c \approx 5\,M_\odot$ (Hartmann 2002; Larson 1985). For comparison, the projected distance between the nearest neighbors of clumps in G049.40−00.01 lies between 0.4 and 2 pc. The mean clump separation is 0.9 pc and the average clump mass is 170 $M_\odot$. Many filamentary IRDCs fragment into clumps with a similar fragmentation scale (Henning et al. 2010; Miettinen & Harju 2010). The difference between the calculated critical mass
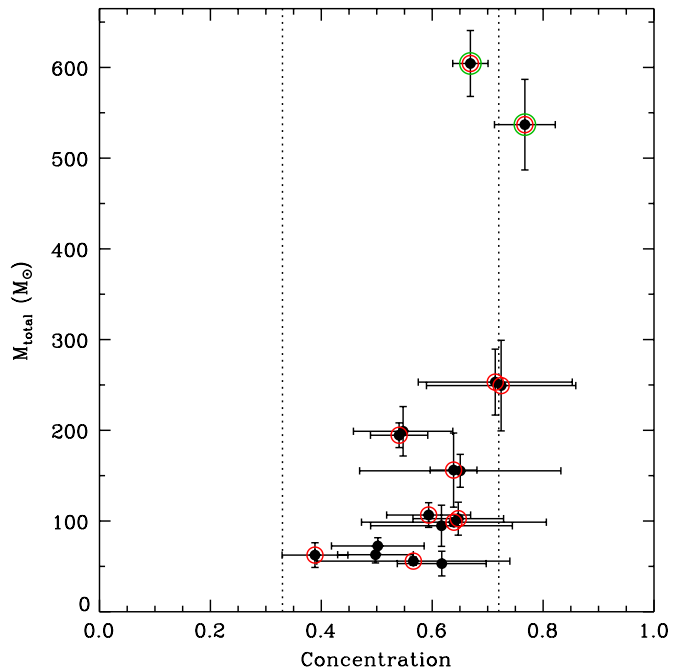

Figure 2. Mass–concentration diagram for the clumps detected in the $350\,\mu$m map. Clumps with large (>0.2) uncertainties in concentration are omitted. Red and green circles represent clumps associated with $24\,\mu$m sources and green fuzzies, respectively (see Section 4.3). The vertical dotted lines ($C = 0.33$ and 0.72) represent the limiting cases of stable Bonnor–Ebert spheres (Johnstone et al. 2000).

and the measured average mass probably indicates that the fragmentation history of G049.40−00.01 is more complicated than the fragmentation of an idealized simple cylinder. Previously suggested possibilities include an extra support by turbulence, changes of cloud temperature, and a compression by external forces (Onishi et al. 1998; Miettinen & Harju 2010).

To study further physical conditions of the clumps, we compare the clumps to a static cloud model. The Bonnor–Ebert model describes the simplest self-gravitating pressure-confined isothermal sphere in a hydrostatic equilibrium (Ebert 1955; Bonnor 1956). The degree of self-gravitation within each clump can be estimated by calculating the degree of concentration of each clump. The concentration can be defined by $C = 1 - R_\Sigma$, where R_Σ is the ratio of average to central column density (see Equation (4) of Johnstone et al. 2000). Small concentrations ($C < 0.33$) imply uniform-density non-self-gravitating objects, and large values ($C > 0.72$) imply critically self-gravitating objects (Johnstone et al. 2000). The concentrations of the submillimeter clumps are listed in Table 3. Figure 2 shows the concentration of the clumps against the clump mass. Most clumps in G049.40−00.01 have concentrations between 0.33 and 0.72. Clump 3 ($C = 0.77 \pm 0.05$) is more concentrated than what is permitted by stable Bonnor–Ebert spheres. In general, massive clumps seem to have high concentrations. It is interesting to note that the four highest-concentration clumps are also the highest-mass ones, and they are all associated with $24\,\mu$m sources, indicating ongoing star formation. Two of them also show signs of shocked gas (see Section 4.3). For the rest of the clumps, there is no clear difference between those with and without $24\,\mu$m sources.

4.3. High-mass Star Formation

Massive stars are expected to be formed in molecular clouds with a large mass concentrated in a relatively small volume.
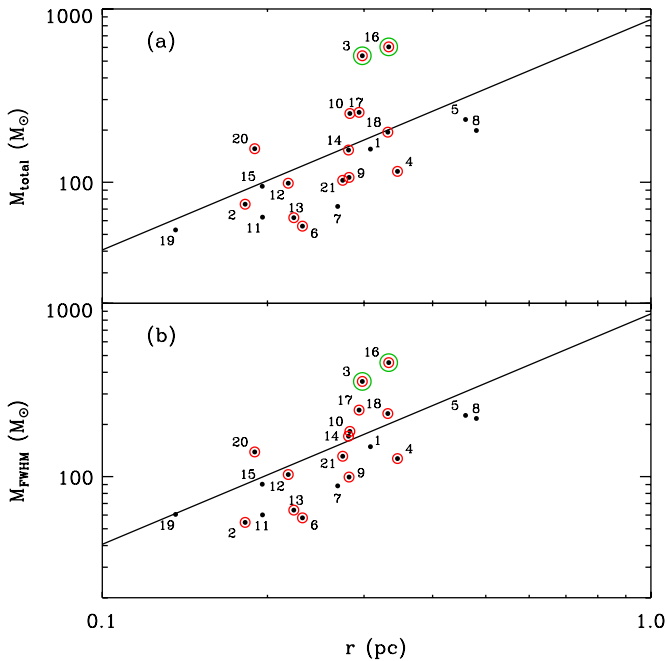
Figure 3. Mass–size diagrams for the clumps detected in the 350 μm map. (a) Mass–size diagram with the total mass given in Table 3. (b) Mass–size diagram with the mass estimated from the flux density within the FWHM boundary (and with the dust opacity scaling factor applied, as suggested by Kauffmann & Pillai 2010). Clumps associated with 24 μm sources are marked by red circles. Two large green circles mark the "green fuzzies." The solid line represents the mass–size threshold for massive star formation, m_{KP}, proposed by Kauffmann & Pillai (2010).

Kauffmann & Pillai (2010) suggested a threshold for massive star formation by comparing clouds with and without massive star formation: $m_{KP} = 870 \, M_{\odot} \, r^{1.33}$, where r is the effective radius (half of the geometric mean of the FWHM sizes in Table 1) in pc. Clouds/clumps more massive than this threshold seem to form massive stars. Parmentier et al. (2011) provided an explanation for the Kauffmann–Pillai threshold by calculating the probable mass of the most massive star formed in model clumps having power-law density profiles.

Figure 3 shows the mass–size relation for the clumps in G049.40–00.01. Kauffmann & Pillai (2010) assumed a dust temperature of 15 K. They used a dust opacity scaled by a factor of 1/1.5 (to match the masses estimated from dust emission and extinction) and a mass correction factor of $1/\ln 2$ (to convert the total mass to the mass contained in the FWHM), and these factors cancel out almost exactly. Figure 3(a) shows the relation between the total mass and the effective radius. Figure 3(b) shows the relation between the mass contained within the FWHM boundary (with the opacity scaled by 1/1.5 to make a proper comparison with Kauffmann & Pillai 2010) and the effective radius. The masses are listed in Table 3. All the clumps are distributed near m_{KP}, within a factor of ~3.5.

Association with bright 24 μm point-like sources is an indicator of star formation because 24 μm emission traces warm dust heated by the material accreting onto a central protostar. Fourteen clumps out of 21 have 24 μm point-like sources within their extent. The most massive ones (clumps 3 and 16) even show extended, enhanced 4.5 μm emission called "green fuzzies" or extended green objects, which indicate shocked gas (Chambers et al. 2009; Cyganowski et al. 2008). Extended 4.5 μm emission also indicates vigorous star-forming activity. In the G049.40–00.01 region, two compact H II regions (PR 29 and 30

in Figure 1(a)) were identified based on *Spitzer* data (Phillips & Ramos-Larios 2008). PR 29 is more extended than PR 30 in the infrared maps (Figures 1(a) and (b)) and is not directly associated with a submillimeter clump. PR 29 seems to be a blister-type H II region formed on the cloud surface near clump 18. In contrast, PR 30 is closely associated with the submillimeter clump 20, which suggests that it is still embedded in the dense cloud. PR 30 may be less evolved than PR 29. Clumps 3, 16, and 20 (clumps associated with "green fuzzies" or compact H II regions) are located well above m_{KP}, and this fact seems to corroborate the threshold for massive star formation suggested by Kauffmann & Pillai (2010).

Several clumps are dark at 24 μm and they may be clumps either in the pre-protostellar phase or containing protostars of undetectably low luminosity. These clumps reside below m_{KP} in Figure 3 and may not be dense enough to form stars (yet). Therefore, objects in various stages of star formation (from pre-protostellar cores, protostars, to H II regions) are distributed in and around the IRDC G049.40–00.01.

Spectral observations would be required to definitively determine the evolutionary status of the clumps. Recent multi-wavelength, high angular resolution studies on IRDCs focused on the chemical, kinematic, and physical properties of the initial conditions for massive star formation. Pillai et al. (2011) investigated secondary massive cold cores in the vicinity of H II regions based on the line (NH$_2$D, NH$_3$, and HCO$^+$) and millimeter continuum observations. They showed that the cores in the earliest stage of massive star formation are cold, dense, and highly deuterated ([NH$_2$D/NH$_3$] > 6%). Devine et al. (2011) found an anti-correlation between NH$_3$ and CCS toward the IRDC G19.30+0.07 based on interferometric observations at 22 GHz. The different evolutionary states of the young objects in G049.40–00.01 can be investigated in detail by obtaining high-resolution interferometric data in the future.

5. SUMMARY

We observed IRDC G049.04–00.01 in the 350 and 850 μm continuum with the SHARC-II bolometer camera. The dark features in the infrared images are in good agreement with the emission structure in the submillimeter images. Twenty-one clumps were identified based on the 350 μm continuum map, and the mass of each clump ranges from 50 to 600 $M_{\odot}$. The majority of these clumps are associated with bright 24 μm emission sources, indicating star-forming activity. The most massive clumps (clumps 3 and 16) show extended, enhanced emission in the IRAC 4.5 μm image. All the clumps are distributed near the threshold for massive star formation. The IRDC G049.04–00.01 contains objects in various evolutionary stages of star formation.

REFERENCES

Battersby, C., Bally, J., Jackson, J. M., et al. 2010, ApJ, 721, 222
Benjamin, R. A., Churchwell, E., Babler, B. L., et al. 2003, PASP, 115, 953
Beuther, H., Churchwell, E. B., McKee, C. F., & Tan, J. C. 2007, in Protostars and Planets V, ed. B. Reipurth, D. Jewitt, & K. Keil (Tucson, AZ: Univ. Arizona Press), 165
Beuther, H., & Henning, T. 2009, A&A, 503, 859
Bonnor, W. B. 1956, MNRAS, 116, 351
Carey, S. J., Clark, F. O., Egan, M. P., et al. 1998, ApJ, 508, 721
Carey, S. J., Feldman, P. A., Redman, R. O., et al. 2000, ApJ, 543, L157
Carey, S. J., Noriega-Crespo, A., Mizuno, D. R., et al. 2009, PASP, 121, 76
Chambers, E. T., Jackson, J. M., Rathborne, J. M., & Simon, R. 2009, ApJS, 181, 360
Cyganowski, C. J., Whitney, B. A., Holden, E., et al. 2008, AJ, 136, 2391
Devine, K. E., Chandler, C. J., Brogan, C., et al. 2011, ApJ, 733, 44
Dowell, C. D., Allen, C. A., Babu, R. S., et al. 2003, Proc. SPIE, 4855, 73
Ebert, R. 1955, Z. Astrophys., 37, 217
Egan, M. P., Shipman, R. F., Price, S. D., et al. 1998, ApJ, 494, L199
Fazio, G. G., Hora, J. L., Allen, L. E., et al. 2004, ApJS, 154, 10
Hartmann, L. 2002, ApJ, 578, 914
Hennemann, M., Birkmann, S. M., Krause, O., et al. 2009, ApJ, 693, 1379
Henning, T., Linz, H., Krause, O., et al. 2010, A&A, 518, L95
Imai, H., Watanabe, T., Omodaka, T., et al. 2002, PASJ, 54, 741
Johnstone, D., Wilson, C. D., Moriarty-Schieven, G., et al. 2000, ApJ, 545, 327
Kang, M., Bieging, J. H., Kulesa, C. A., et al. 2010, ApJS, 190, 58
Kang, M., Bieging, J. H., Povich, M. S., & Lee, Y. 2009, ApJ, 706, 83
Kauffmann, J., & Pillai, T. 2010, ApJ, 723, L7
Kovács, A. 2006, PhD thesis, California Institute of Technology
Lada, C. J., & Lada, E. A. 2003, ARA&A, 41, 57
Larson, R. B. 1985, MNRAS, 214, 379
Leong, M., Peng, R., Houde, M., et al. 2006, Proc. SPIE, 6275, 21
Miettinen, O., & Harju, J. 2010, A&A, 520, A102
Onishi, T., Mizuno, A., Kawamura, A., Ogawa, H., & Fukui, Y. 1998, ApJ, 502, 296
Ossenkopf, V., & Henning, T. 1994, A&A, 291, 943
Parmentier, G., Kauffmann, J., Pillai, T., & Menten, K. M. 2011, MNRAS, 416, 783
Peretto, N., & Fuller, G. A. 2009, A&A, 505, 405
Peretto, N., Fuller, G. A., Plume, R., et al. 2010, A&A, 518, L98
Phillips, J. P., & Ramos-Larios, G. 2008, MNRAS, 391, 1527
Pillai, T., Kauffmann, J., Wyrowski, F., et al. 2011, A&A, 530, A118
Rathborne, J. M., Jackson, J. M., Chambers, E. T., et al. 2005, ApJ, 630, L181
Rathborne, J. M., Jackson, J. M., & Simon, R. 2006, ApJ, 641, 389
Rieke, G. H., Young, E. T., Engelbracht, C. W., et al. 2004, ApJS, 154, 25
Sato, M., Reid, M. J., Brunthaler, A., & Menten, K. M. 2010, ApJ, 720, 1055
Simon, R., Jackson, J. M., Rathborne, J. M., & Chambers, E. T. 2006a, ApJ, 639, 227
Simon, R., Rathborne, J. M., Shah, R. Y., Jackson, J. M., & Chambers, E. T. 2006b, ApJ, 653, 1325
Stutz, A., Launhardt, R., Linz, H., et al. 2010, A&A, 518, L87
Wilcock, L. A., Kirk, J. M., Stamatellos, D., et al. 2011, A&A, 526, A159
Xu, Y., Reid, M. J., Menten, K. M., et al. 2009, ApJ, 693, 413